Nano Research 2017, 10(6): 2056–2069
DOI 10.1007/s12274-016-1395-0
Research Article
ISSN 1998-0124
CN 11-5974/O4

Porous Pt/Ag nanoparticles with excellent multifunctional enzyme mimic activities and antibacterial effects

Shuangfei Cai[1], Xinghang Jia[1], Qiusen Han[1], Xiyun Yan[2], Rong Yang[1] (✉), and Chen Wang[1] (✉)

[1] *CAS Center for Excellence in Nanoscience, National Center for Nanoscience and Technology, University of Chinese Academy of Sciences, Beijing 100190, China*
[2] *Key Laboratory of Protein and Peptide Pharmaceutical, National Laboratory of Biomacromolecules, Institute of Biophysics, Chinese Academy of Sciences, Beijing 100101, China*

Received: 30 September 2016
Revised: 24 November 2016
Accepted: 28 November 2016

KEYWORDS
platinum,
porous,
oxygen reduction reaction,
enzyme mimic,
antibacterial

ABSTRACT

Enhancing the activity of Pt-based nanocatalysts is of great significance yet a challenge for the oxygen reduction reaction (ORR). In this work, a series of porous Pt/Ag nanoparticles (NPs) were fabricated from regular Pt_xAg_{100-x} (x = 25, 50, 75) octahedra by a facile and economical dealloying process. Remarkable enhancement in multiple enzyme-mimic activities related to ORR was observed for the dealloyed $Pt_{50}Ag_{50}$ (D-$Pt_{50}Ag_{50}$) NPs. This effect can be attributed to the resulting Pt-rich surface structure, increased surface area, and a synergistic effect of Pt and Ag atoms in the D-$Pt_{50}Ag_{50}$ NPs. Furthermore, the D-$Pt_{50}Ag_{50}$ NPs exerted excellent antibacterial effects on two model bacteria (gram-negative *Escherichia coli* and gram-positive *Staphylococcus aureus)*. The present work represents a significant advance in the exploration of the relation between controllable synthesis of high-quality nanoalloys and their novel catalytic properties for various promising applications, including catalysts, biosensors, and biomedicine.

1 Introduction

The oxygen reduction reaction (ORR), as an important cathode reaction, is widely employed in fuel cells and metal-air batteries for renewable-energy applications [1–3]. For many years, various Pt-based nanocatalysts with well-defined shapes and controllable facets have been extensively studied [4–14], aimed at enhancing the ORR activity.

Recently, dealloyed Pt-based bimetallic nanoparticles (NPs) have attracted considerable attention as electrocatalysts for ORR [15–19]. The chemical or electrochemical dealloying treatment leads to a change in the arrangement and configuration of the surface and/or topmost few layers of Pt atoms, which dramatically affect the adsorption and activation of oxygen, accompanied by enhancement of ORR activity. Depending on the structure of bimetallic NPs as templates, several typical examples include production of ultrathin icosahedral Pt-enriched nanocages from

Address correspondence to Rong Yang, yangr@nanoctr.cn; Chen Wang, wangch@nanoctr.cn

PdPt core–shell NPs [20], construction of a Pt-skin structure on the FePt and CoPt alloy nanowires [21], and formation of thin Pt skin (ca. 1 nm in thickness) on the Cu_3Pt/C intermetallic NPs [22]. Nonetheless, extension of this facile and economical method to high-quality nanoalloys and their novel catalytic properties still lack due research.

An octahedron, which is one of the simplest platonic solids, is composed of 8 equilateral triangle faces. Owing to many intriguing properties such as high symmetry, the existence of critical edges and complete {111} facets, face-centered cubic (fcc) metal nano-octahedra [23–27] have previously been used as typical models for catalysis (e.g., hydrogenation and ORR), photonics, and surface-enhanced Raman spectroscopy (SERS) studies. Meanwhile, nanoporous materials have found broad applications in catalysis involving ORR, resulting from their large surface area, low density, and high catalytic efficiency [28–32]. Thus, nanoporous octahedra could be anticipated to show greatly enhanced ORR activity.

Herein, we report a series of porous Pt/Ag NPs obtained by chemical dealloying of regular Pt_xAg_{100-x} ($0 < x < 100$) octahedra. By means of the dealloying process, some Ag atoms are selectively removed, producing the Pt-enriched surface structure with increased surface area. Remarkable enhancement in ORR-related activities of the dealloyed $Pt_{50}Ag_{50}$ NPs as multifunctional enzyme mimics was observed: oxidase- and peroxidase-like activities in the oxidation of 3,3',5,5'-tetramethylbenzidine (TMB) as a classic chromogenic substrate as well as catalase-like activity in the decomposition of hydrogen peroxide (H_2O_2) to water and oxygen. Besides, the dealloyed $Pt_{50}Ag_{50}$ NPs have excellent antibacterial effects on two model bacteria (*Escherichia coli* (*E. coli*) and *Staphylococcus aureus* (*S. aureus*)). Based on these fascinating observations, the dealloyed Pt/Ag NPs demonstrate a great potential for various important applications in catalysis, biosensing, and biomedicine.

2 Experimental

2.1 Materials

Polyallylamine hydrochloride (PAH, molecular weight 120,000 to 200,000), 3-carbamoyl-2,2,5,5-tetramethyl-3-pyrroline-1-yloxyl (CTPO), and silver nitrate ($AgNO_3$) were supplied by Alfa Aesar. Chloroplatinic acid hexahydrate ($H_2PtCl_6{\cdot}6H_2O$) was provided by J&K Scientific Ltd. (Beijing, China). TMB was obtained from Acros and catalase (from bovine liver) was bought from TCI. A formaldehyde (HCHO) solution (40%) was purchased from Xilong Chemical Co., Ltd. (Shantou, China). H_2O_2 solution (30%) and nitric acid (HNO_3) solution (65%–68%) were provided by Beijing Chemical Works (Beijing, China). Other reagents and chemicals were at least analytical-reagent grade. Ultrapure water was prepared by means of a Milli-Q ultrapure system (18 MΩ·cm).

2.2 Characterization

Transmission electron microscopy (TEM) images of NPs were obtained using a transmission electron microscope (FEI Tecnai G2 20 S-TWIN) operating at an accelerating voltage of 200 kV. The crystalline structure and phase purity were determined using an X-ray powder diffractometer (XRD, Bruker D8 focus) with Cu Kα radiation (λ = 1.5406 Å) at room temperature and a high-resolution transmission electron microscope (HRTEM, JEM-2010F). Partial images were collected under a transmission electron microscope (FEI Tecnai G2 F20 U-TWIN). The composition of the products was analyzed by the inductively coupled plasma optical emission spectrometer (ICP-OES, Thermo Scientific iCAP 6300), and energy dispersive X-ray spectrometer (EDX) analysis. UV–Vis absorption spectroscopic measurements were carried out using a UV/Vis spectrophotometer (PerkinElmer Lambda 950) and a multimode plate reader (PerkinElmer EnSpire®). Zeta potential was measured using a Malvern Zetasizer Nano system. Brunauer–Emmett–Teller (BET) measurements were conducted on an ASAP2020 (M+C) surface area analyzer. X-ray photoelectron spectra (XPS) were recorded using an X-ray photoelectron spectrometer (Thermo Fisher ESCALAB 250Xi). Binding energies (BE) were calibrated by setting the measured BE of C 1s to 284.8 eV. Electron spin resonance (ESR) spectra were recorded at room temperature on a JEOL JES-FA200 ESR spectrometer. All the photos were taken by means of a Canon camera.

2.3 Preparation of Pt/Ag NPs

By changing the molar ratio between the metal precursors of chloroplatinic acid hexahydrate and silver nitrate, a series of octahedral Pt_xAg_{100-x} ($0 < x < 100$) NPs were prepared, where x represents the molar percentage of Pt atoms. For example, in the synthesis of $Pt_{50}Ag_{50}$ NPs, 122 μL of $AgNO_3$ (0.0492 M), 236.2 μL of $H_2PtCl_6{\cdot}6H_2O$ (0.0254 M), and 200 μL of HCHO were added to 4 mL of a PAH solution (10 mg·mL^{-1}), followed by 10 min of vigorous stirring. The resulting homogeneous solution was transferred into a 10-mL Teflon-lined stainless-steel autoclave. The sealed vessel was then heated at 200 ℃ for 4 h before it was cooled down to room temperature. The final product was separated by centrifugation, washed with ultrapure water, and then dispersed into 4 mL of ultrapure water to obtain a stock solution.

Porous Pt/Ag NPs were obtained by the chemical dealloying method. Briefly, 1 mL of the stock solution of Pt/Ag NPs was etched with 4 mL of HNO_3 solution at room temperature under ultrasonic condition (frequency 40 kHz). When the required etching time was completed, the samples were then immersed in deionized water for several minutes to stop the dealloying process and remove the residual nitric acid.

2.4 Catalytic activity test

The oxidase- or peroxidase-like activity of dealloyed Pt/Ag NPs was investigated through TMB oxidation without or with H_2O_2 to generate a colorimetric reaction with a total volume of 500 μL. Typically, the reactions were carried out in acetate buffer (0.2 M, pH 4.0) using 10 μL of dispersion of dealloyed Pt/Ag (1 mM based on total metals) and 10 μL of TMB (50 mM) in the absence or presence of 10 μL of H_2O_2 (50 mM). After incubation for 10 min at room temperature, the absorbance of the resulting solution at 652 nm was determined immediately.

The catalase-like activity of dealloyed Pt/Ag NPs was studied with H_2O_2 decomposition to form oxygen and water. Typically, a stock solution containing CTPO, a water-soluble spin label and H_2O_2 was first deoxygenated with N_2. After that, the catalase (1 mg·mL^{-1}, 5 μL) or Pt/Ag NPs (1 mM based on metals, 10 μL) were added. Then the as-prepared samples were transferred into 50-μL glass capillary tubes, sealed, and placed in the ESR compartment. Final concentrations were 0.1 mM CTPO and 0.25 mM H_2O_2 in 50 mM phosphate buffer saline (PBS) (pH 7.4). ESR experiments were run by a JEOL JES-FA200 spectrometer. ESR signals were obtained with 2 mW incident microwave power, 0.06 G field modulation, sweep width 2.5 G, and time constant of 0.03 s.

2.5 Analysis of antibacterial effects

Gram-negative bacteria *E. coli* (ATCC25922) and the gram-positive bacteria *S. aureus* (ATCC6538) were cultured in lysogeny broth (LB) medium at 37 ℃ overnight at a rotation speed of 150 rpm. Then, the cultures were centrifuged at 5,000 rpm for 5 min. The bacteria were washed with 1× PBS twice to remove growth medium constituents. Later, the bacteria were resuspended in 1× PBS to final concentration of 10^8 CFU·mL^{-1}, serving as a bacterial stock suspension.

A mixture of 10 μL of the bacterial stock suspension and H_2O_2 at different concentrations was incubated at 37 ℃ for 12 h in a 96-well microplate. The proliferation ability of bacteria treated with H_2O_2 was determined by recording absorption of the solutions at 600 nm. The suspension of dealloyed $Pt_{50}Ag_{50}$ NPs was sonicated (100 W, 40 kHz, 10 min) before dilution with 1× PBS to the desired test concentrations (5–20 μg·mL^{-1}). After that, 10 μL of a bacterial suspension was mixed with suspension of dealloyed $Pt_{50}Ag_{50}$ and H_2O_2 (10 or 200 μM for *E. coli* and *S. aureus*, respectively), followed by incubation at 37 ℃ for 2 h during 150 rpm rotation. Then, 20 μL of the bacterial suspension with 10-fold dilution was spread on the solid medium and further incubated at 37 ℃ for 24 h. The antimicrobial activity of dealloyed $Pt_{50}Ag_{50}$ NPs was determined by counting the bacterial colonies.

2.6 Lipid peroxidation measurements and a lactate dehydrogenase (LDH) release assay

As an indicator of lipid peroxidation, malondialdehyde (MDA) was tested. Typically, reagents of the MDA Assay Kit were added in a row according to the manufacturer's instructions, and absorbance was recorded at 535 nm. Protein concentrations were quantified by an Enhanced BCA Protein Assay Kit.

After exposure to NPs, the bacteria were lysed in lysis buffer at 4 ℃ for 30 min. Then, BCA working solution was added to each well and incubated at 37 ℃ for 30 min. The absorbance was recorded at 450 nm.

Intracellular contents would be released outside if cell membrane was broken, and a LDH release assay kit was used to evaluate bacterial membrane integrity. Briefly, the bacterial stock suspension was first incubated with dealloyed $Pt_{50}Ag_{50}$ (20 μg·mL^{-1}) and H_2O_2 (10 or 200 μM) for 2 h. Then, the supernatant was collected by centrifugation at 5,000 rpm for 5 min. After the reagents of LDH assay kit were added, the absorbance was recorded at 450 nm.

3 Results and discussion

3.1 Synthesis and characterization of porous Pt/Ag NPs

In a typical synthesis, a series of monodisperse and homogeneous Pt_xAg_{100-x} ($0 < x < 100$) NPs were fabricated by the hydrothermal method, where $H_2PtCl_6{\cdot}6H_2O$ and $AgNO_3$ served as precursors, formaldehyde as a reducing agent, and PAH as a surfactant. Figure S1 in the Electronic Supplementary Material (ESM) shows typical TEM images of the as-prepared $Pt_{75}Ag_{25}$, $Pt_{50}Ag_{50}$, and $Pt_{25}Ag_{75}$ NPs, whose morphology is octahedral and the average edge length was found to be in the range of 20.9 to 22.1 nm. The EDX spectroscopy analysis and ICP-OES confirmed that the Pt/Ag atomic ratios were close to the designed composition of Pt_xAg_{100-x} NPs (Table S1 in the ESM). The XRD patterns show that these octahedral NPs exhibit a fcc structure (Fig. S2 in the ESM). The diffraction peaks gradually shift toward a lower angle as the Ag content increases, which is due to the increase in the lattice constant by alloying Pt with Ag. Collectively, Pt/Ag octahedra with different Pt/Ag molar ratios were successfully synthesized. Furthermore, we studied the effects of reaction conditions such as temperature and surfactant concentration on the edge length of the NPs. The results are shown in Fig. S3 in the ESM where $Pt_{50}Ag_{50}$ NPs were chosen as an example.

Subsequently, the as-prepared Pt_xAg_{100-x} ($0 < x < 100$) octahedra were dealloyed with nitric acid at room temperature for 15 min. The products are hereafter referred to as D-$Pt_{75}Ag_{25}$, D-$Pt_{50}Ag_{50}$, and D-$Pt_{25}Ag_{75}$, respectively. The edge length (EL) of products mainly relies on the Pt/Ag octahedra as templates (see Fig. S4 in the ESM). A typical TEM image of the D-$Pt_{50}Ag_{50}$ NPs with average EL of 34.5 nm is shown in Fig. 1(a), which displays an octahedron-like shape with a lot of well-defined mesopores.

According to the BET measurements, the surface area of D-$Pt_{50}Ag_{50}$ NPs is 12.11 ± 0.11 m^2·g^{-1}, larger than that of $Pt_{50}Ag_{50}$ NPs (5.04 ± 0.11 m^2·g^{-1}). The mesoporous characteristics can also be more clearly observed in a HRTEM image of a single Pt/Ag porous particle (Fig. 1(b)), owing to its high pore volume fraction (ca. 59% v/v). The crystalline structure of D-$Pt_{50}Ag_{50}$ was measured by XRD. The diffraction peaks (Fig. 1(c)) at 2θ values of 39.19°, 45.57°, 66.33°, 79.64°,

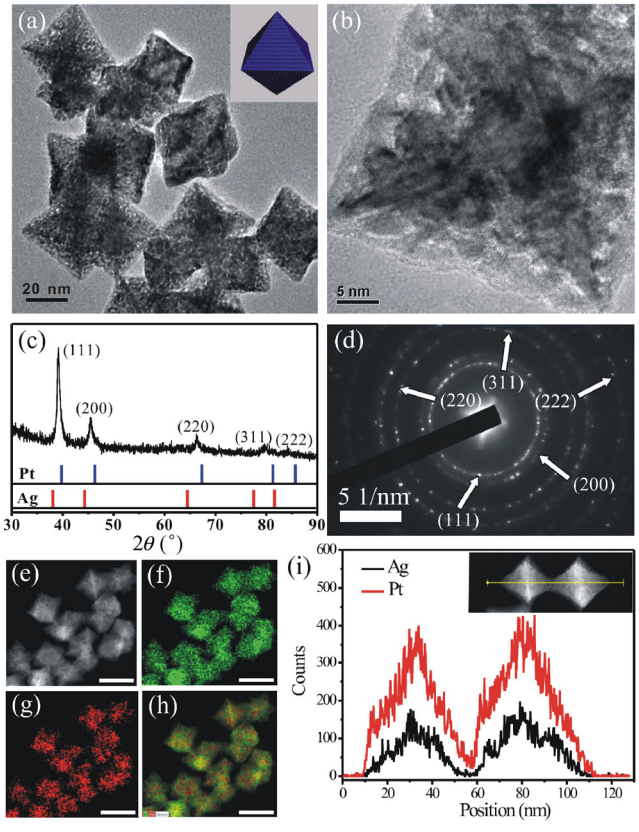

Figure 1 (a) A TEM image (inset: illustration), (b) HRTEM image, (c) an XRD pattern, (d) SAED pattern, (e) HAADF-STEM image, elemental maps for (f) Pt, (g) Ag, and (h) overlapped elemental maps of Pt and Ag (scale bar: 50 nm), (i) EDX line-scanning profile across two Pt/Ag particles of D-$Pt_{50}Ag_{50}$.

and 84.15° can be assigned to the (111), (200), (220), (311), and (222) crystal planes of D-$Pt_{50}Ag_{50}$ NPs with an fcc structure, respectively, which is in good accord with the corresponding selected area electron diffraction (SAED) pattern (Fig. 1(d)). The diffraction peaks were positioned between the standard peaks of Pt (JCPDS, 04-0802) and Ag (JCPDS, 04-0783), showing the bimetallic phase of Pt and Ag. Notably, compared with those of $Pt_{50}Ag_{50}$ NPs (see Fig. S2(d) in the ESM), all the peaks are slightly shifted to larger 2θ values (d-spacing decreases) after corrosion, resulting from partial removal of Ag atoms with larger crystal lattice. To further investigate the nanostructure of porous Pt/Ag NPs, the element distributions of Pt and Ag in the sample were studied by a high-angle, annular dark-field scanning transmission electron microscope (HAADF-STEM). Figure 1(e)–1(g) shows the representative STEM image and corresponding elemental maps, respectively. From the overlapping element map of Pt and Ag (Fig. 1(h)), one can see that the Pt element is mainly distributed in the outer layer of each individual NP. The Pt-enriched structure is supported by the line-scanning profile across two single Pt/Ag particles (Fig. 1(i)), in which the intensity of Ag is far lower than that of Pt in the outer layer. The EDX analysis (see Fig. S5(a) in the ESM) of porous NPs gave a Pt/Ag molecule ratio of 60.5:39.5, which is in good agreement with the ICP-OES containing 59.7% of Pt and 40.3% of Ag.

To further reveal the Pt-enriched structure, the surface composition and chemical state of D-$Pt_{50}Ag_{50}$ NPs were confirmed by XPS. The calculated atomic concentrations of Pt and Ag from the XPS survey scan spectra (see Fig. S5(b) in the ESM) are 14.68% and 4.08% with a ratio of 3.6:1, which is larger than that of $Pt_{50}Ag_{50}$ NPs (1.3:1). The result suggests that the surface of D-$Pt_{50}Ag_{50}$ NPs mainly contains Pt atoms, verifying again the observations from the STEM image and line-scanning profile. The high-resolution Pt 4f XPS spectra can be fitted well into two individual doublets (see Fig. S5(c) in the ESM). The two peaks at 70.7 and 74.1 eV are attributed to the Pt $4f_{7/2}$ and Pt $4f_{5/2}$ binding energies for Pt^0, respectively [33]. Meanwhile, Ag 3d spectrum shows two peaks located at 367.8 and 374.0 eV (see Fig. S5(d) in the ESM), which are characteristic of the Ag $3d_{3/2}$ and Ag $3d_{5/2}$ components of Ag^0, respectively [34]. By measuring the relative peak area, we found that Ag^+ is the main species in the dealloyed $Pt_{50}Ag_{50}$ NPs. Thus, the D-$Pt_{50}Ag_{50}$ NPs were successfully obtained.

3.2 The mechanism of the dealloying process

In principle, when silver is placed in nitric acid, Ag^0 is oxidized to Ag^+ and HNO_3 reduced into NO_2 gas simultaneously. By such a free corrosion process, partial Ag atoms are selectively removed from Pt/Ag octahedra. To gain a better understanding of the dealloying process, we studied the dissolution kinetics of Ag upon immersion of Pt/Ag octahedra in nitric acid at room temperature. Knowing the initial Ag content within the Pt/Ag octahedra (x_0) and the one after specific etching time (x_t) by *ex situ* EDX analysis, the fraction of Ag dissolved in nitric acid (c_{Ag}) can be calculated as follows

$$c_{Ag}\ (\%) = \frac{x_0 - x_t}{x_0} \times 100 \quad (1)$$

As shown in Fig. 2(a), for the three types of Pt_xAg_{100-x} octahedra selected in this study, the dissolved amount of Ag in nitric acid increases as the dealloying process progresses. For $Pt_{25}Ag_{75}$ octahedra, ~55% of Ag atoms from octahedra were removed during the first 30 s of exposure to nitric acid; this phenomenon indicates that Ag dissolves rapidly during the early stage of etching. After 30 s of dealloying, the typical HAADF-STEM image shown in Fig. 2(b) confirms the porous feature of dealloyed Pt/Ag NPs. From the three EDX line-scanning profiles across a single randomly selected Pt/Ag particle (Figs. 2(c)–2(e)), the atomic ratios of Pt/Ag were found to be 67:33, 64:36, and 66:34, respectively. These results indicate that there is no obvious difference in the composition along different directions. Between 1 and 5 min, the dissolution kinetics of Ag gradually slow down. If we increase etching time further, the dissolution kinetics of Ag reach a plateau. On the contrary, for Pt/Ag octahedra with initial Pt content higher than 25 at.%, the dissolution kinetics of Ag were found to be much slower. In the range of 2 to 30 min, the increase in the amount of dissolved Ag is negligible. After 30 min of dealloying,

only ~20% of the initial Ag atoms are removed from octahedra. A similar observation was reported by El Mel et al. for the dealloying of Au/Cu NPs in HNO_3 [35]. In their experiments, when the initial Au content was higher than 24%, the dissolution kinetics of Cu decreased greatly, likely due to the local passivation of the alloy surface by the formed Au clusters. These noble-metal clusters are formed as a result of the surface migration and coalescence of the less coordinated Au atoms. The decrease in dissolution kinetics of Ag in our study can be explained by the local passivation of surface by the formed Pt clusters. Especially, when the initial Pt content within the octahedra was higher, the surface passivation effect was expected to become more important. In another words, the initial Pt content in octahedra plays an essential role in the dissolution kinetics of Ag, where the lower the initial Pt content, the greater is the extent of Ag dissolution.

Nonetheless, for all the experiments, the dealloying process did not result in complete removal of silver. The changed atomic ratio of Ag is shown in Fig. 3(a). The composition of the D-$Pt_{75}Ag_{25}$ and D-$Pt_{25}Ag_{75}$ NPs was found to be $Pt_{79}Ag_{21}$ and $Pt_{90}Ag_{10}$, respectively. This result is consistent with XRD data shown in Fig. 3(b) because the diffraction peak located in the (111) plane shifts to higher angles, which means that the proportion of Pt within the dealloyed NPs increases.

To further understand the formation of porous Pt/Ag NPs, the morphological evolution of Pt/Ag octahedra as a function of etching time was studied. For clear

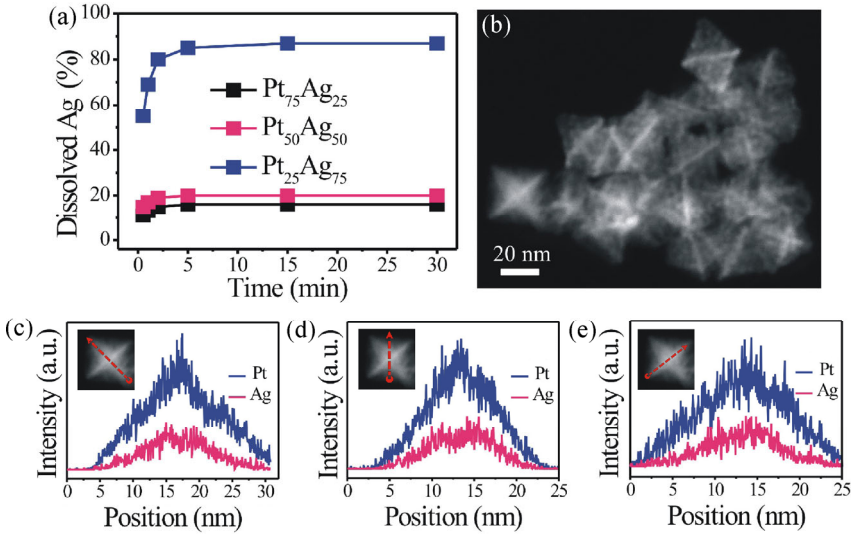

Figure 2 (a) Evolution of the dissolved amount of Ag as a function of the dealloying time, (b) a HAADF-STEM image and (c)–(e) EDX line-scanning profiles across a single particle along different directions of D-$Pt_{25}Ag_{75}$ after 30 s of etching.

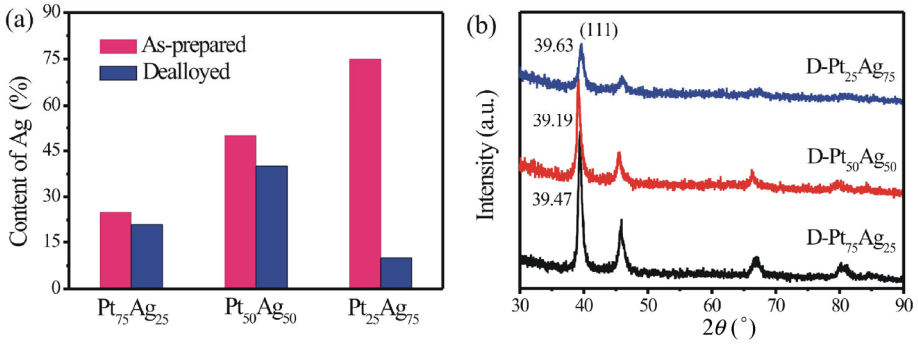

Figure 3 (a) Composition changes before and after dealloying of Pt_xAg_{100-x} NPs determined by EDX analysis; (b) XRD patterns of the dealloyed Pt_xAg_{100-x} NPs.

demonstration of this issue, we selected $Pt_{25}Ag_{75}$ octahedra with high initial content of Ag. As shown in Fig. 4(a), the particle before dealloying possesses continuous lattice fringes on the {111} faces. One can see that, after 0.5 min of dealloying, several small pores and cracks appear on the particle, producing a rough surface (Fig. 4(b)). Increasing etching time to 1 min, the pores become more and more obvious while the lattice fringes are discrete (Fig. 4(c)). As the reaction continues, the pore size increases (Fig. 4(d)). Unlike D-$Pt_{50}Ag_{50}$ NPs (Fig. 1(b)), one can notice that the initial complete {111} faces of $Pt_{25}Ag_{75}$ NPs disappear after dealloying for 15 min while the octahedral nanoframes form. These data indicate that both etching time and initial composition have a strong influence on the morphology of Pt/Ag NPs. The understanding of the effects of dealloying conditions and alloy composition on the morphological changes of Pt/Ag NPs would be useful for further research.

On the basis of the above results, one can conclude that Ag atoms rapidly dissolve from the surface of Pt_xAg_{100-x} octahedra at the beginning of the dealloying process. The particle surface becomes rough as several small pores appear. With increasing removal of Ag atoms from the top layer, Ag atoms start to move from the particle's inner part toward the particle surface, while the pores increase. Considering a slow Ag bulk diffusion compared to a fast surface Ag dissolution, the dissolution of Ag decelerates as the reaction goes on. Finally, the particle surface depletes to a relatively low concentration of Ag, leading to formation of the Pt-enriched structure with porous characteristics.

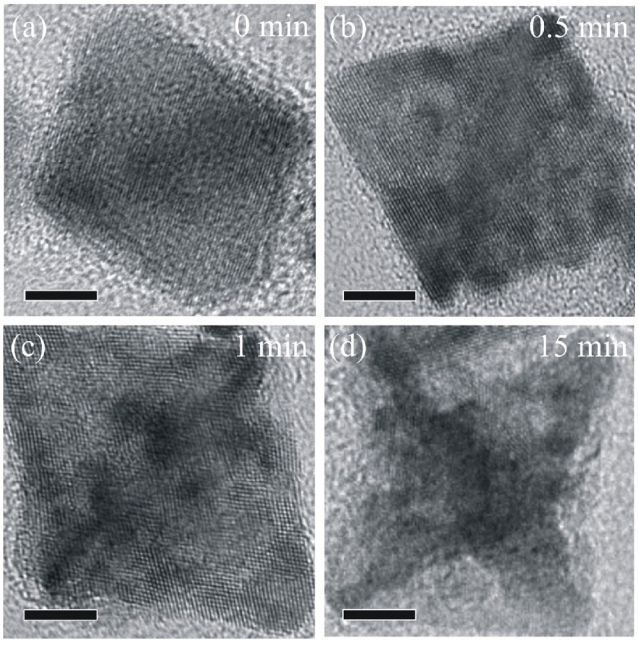

Figure 4 The impact of dealloying time on the morphology of $Pt_{25}Ag_{75}$ NPs. Scale bar: 5 nm.

3.3 Catalytic properties of the dealloyed Pt/Ag NPs

With dealloyed materials in hand, the possible catalytic properties of Pt/Ag NPs were systematically investigated.

The oxidation of TMB, a classical chromogenic substrate has widely been used to study the oxidase- and/or peroxidase-like activity of NP-based enzyme mimics [36–38], was chosen as a model reaction. To our delight, the D-$Pt_{50}Ag_{50}$ NPs with average edge length of 34.5 nm as a model catalyst can drive the oxidation of TMB at room temperature, producing a typical blue color by dissolved oxygen or H_2O_2 (Figs. 5(a) and 5(b)). In contrast, the control experiments without material show negligible color variation. Thus, D-$Pt_{50}Ag_{50}$ NPs have oxidase- and peroxidase-like activities. Compared with $Pt_{50}Ag_{50}$ NPs, meanwhile, D-$Pt_{50}Ag_{50}$ gives deeper blue color (Figs. 5(a)(3) and Fig. 5(b)(4)) with higher absorbance at 652 nm (Fig. 5(c)), a characteristic absorption peak of oxidized TMB.

To study the structure-activity relation, the TMB oxidation reactions with H_2O_2 were conducted using Pt/Ag NPs with different molar ratios of Pt/Ag. For comparison, all the catalysts were kept at the same edge length of ~35 nm. As shown in Fig. 5(d), all the dealloyed Pt/Ag NPs display better performance than the counterpart alloyed ones. The enhanced activity of Pt/Ag NPs after dealloying can be attributed to the increased surface area and active sites. It is believed that the reaction goes through a pathway similar to the electrochemical reduction of oxygen or H_2O_2 using Pt as an electrocatalyst [39–41]. In contrast to the way electrons are provided in electrochemistry (via applied voltage), the electrons herein come from TMB molecules. The abundant active sites on the D-$Pt_{50}Ag_{50}$ NPs with Pt-enriched structure facilitate the adsorption of dissolved oxygen and H_2O_2 as electron acceptors. Meanwhile, TMB molecules are readily absorbed on the surface of D-$Pt_{50}Ag_{50}$ NPs

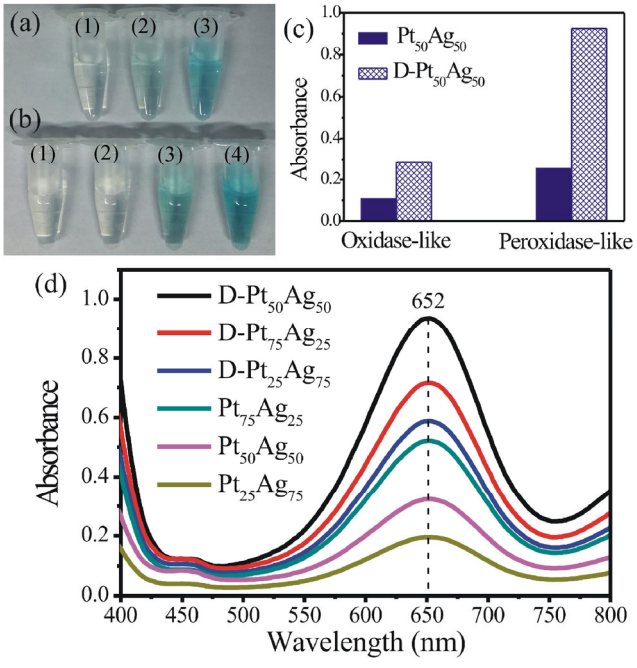

Figure 5 (a) TMB oxidation in air: (1) TMB; (2) mixed with $Pt_{50}Ag_{50}$; (3) mixed with D-$Pt_{50}Ag_{50}$; (b) TMB oxidation with H_2O_2: (1) TMB; (2) mixed with H_2O_2; (3) mixed with $Pt_{50}Ag_{50}$ and H_2O_2; (4) mixed with D-$Pt_{50}Ag_{50}$ and H_2O_2; (c) comparison of activities of Pt/Ag in TMB oxidation and (d) catalytic oxidation of TMB by different Pt/Ag NPs.

owing to the large surface area. With electron transfer from TMB molecules to D-$Pt_{50}Ag_{50}$ NPs, rapid reduction of the adsorbed oxygen or H_2O_2 on the NP surface and oxidation of TMB molecules occurred simultaneously (Fig. 6).

Besides, for the three types of dealloyed Pt/Ag catalysts, the highest activity was observed at an initial Ag composition of 50%, which suggests that the alloy composition plays a critical role in catalytic activity during TMB oxidation. The highest residual content of Ag in the D-$Pt_{50}Ag_{50}$ catalyst coincides well with its highest activity, which is consistent with other reports describing electrocatalysis for ORR by the dealloyed Au/Cu and Pt/Ni NPs [35, 42]. The high activity can be explained as a synergistic effect of Pt and the residual Ag atoms in the D-$Pt_{50}Ag_{50}$ catalyst. It is known that Pt and Ag have electronegativity values of 2.28 and 1.93, respectively. With high electronegativity difference (0.32) between them, some of the electrons in Ag can transfer into the d-orbital of Pt, and this change could result in filling in the Pt d-band and downshifting the d-band center energy. Therefore, the

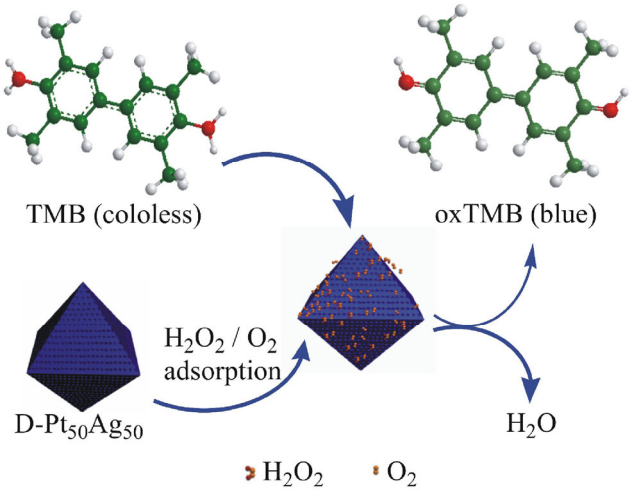

Figure 6 Schematic illustration of TMB oxidation by D-$Pt_{50}Ag_{50}$.

D-$Pt_{50}Ag_{50}$ NPs with the highest content of residual Ag yield the best catalytic activity. Additionally, after we changed the average EL of D-$Pt_{50}Ag_{50}$ NPs from 19.2 to 34.5 nm (Fig. S4 in the ESM), no remarkable difference in the activity was observed for TMB oxidation. Thus, D-$Pt_{50}Ag_{50}$ NPs with average edge length of 34.5 nm were selected for further experiments.

Several factors affecting the catalytic activities of D-$Pt_{50}Ag_{50}$ NPs in TMB oxidation were also studied. Similar to other NPs [43, 44], the activities of D-$Pt_{50}Ag_{50}$ NPs showed pH and temperature dependence (see Fig. S6 in the ESM). Under the present experimental conditions, the optimal pH and temperature were 4.0 and 40 °C, respectively. For practical applications, the stability of a catalyst is an essential issue. The D-$Pt_{50}Ag_{50}$ NPs were found to be well dispersed in water (Fig. S7 in the ESM). The measured surface zeta-potential of D-$Pt_{50}Ag_{50}$ NPs in water (pH 6.5) was 36.8 mV; therefore, they have good stability. Moreover, when the NP dispersion was stored at room temperature for weeks, no obvious decrease in the response to H_2O_2 was observed. The result suggests that the D-$Pt_{50}Ag_{50}$ NPs have high catalytic stability. Thus, these advantages make these NPs suitable and practical for a broad range of applications.

To further reveal peroxidase-like activity of D-$Pt_{50}Ag_{50}$ NPs, the steady-state kinetic experiment was performed (see Fig. S8 in the ESM). The Michaelis–Menten constant (K_m) and maximum initial rate (V_{max}) can be obtained from a Lineweaver–Burk plot, and the lower apparent K_m value means higher affinity of substrates

for enzymes. As shown in Table 1, the V_{max} values for D-$Pt_{50}Ag_{50}$ NPs are 2- to 3-fold larger than those for $Pt_{50}Ag_{50}$ NPs. These values are also higher than those of horseradish peroxidase (HRP) [36] and several known NP-based peroxidase mimics [44–49]. Meanwhile, compared to HRP, the K_m value for D-$Pt_{50}Ag_{50}$ NPs with H_2O_2 as a substrate is lower. The higher rate and affinity can be explained as follows: D-$Pt_{50}Ag_{50}$ NPs have a large surface area and more active sites, while an HRP molecule contains only one iron ion that decomposes H_2O_2.

The decomposition of H_2O_2, which has received much research attention in water treatment [50–52], was used as another probe reaction for the redox catalytic activity of dealloyed NPs. It was found that H_2O_2 can be rapidly decomposed by D-$Pt_{50}Ag_{50}$ to generate gas bubbles under present conditions (see Experimental section). To examine whether the bubbles could be gas oxygen related to the catalase-like activity of D-$Pt_{50}Ag_{50}$ NPs, a series of ESR experiments were conducted in a closed chamber with samples. To quantify the evolution of oxygen concentration, a parameter K that reflects the change in super hyperfine structure in ESR spectra was used [53], which was calculated by means of the equation $K = (h_1 + h_2)/2h$, where h_1, h_2, and h are determined as shown in Fig. 7(a).

The obtained K values for catalase and $Pt_{50}Ag_{50}$ NPs for comparison are 0.144 and 0.186, respectively. In contrast, D-$Pt_{50}Ag_{50}$ NPs yield a value of K at 0.105. This result suggests that the dealloyed NPs possess higher activity.

As previously proposed, the decomposition of H_2O_2 by Pt-based bimetallic NPs such as PtPd NPs proceeds via the surface-catalyzed mechanism [54]. In our study, the process can be described as follows. The first step

Table 1 Comparison of the apparent K_m and the V_{max} between Pt/Ag NPs and HRP

Catalyst	Substrate	K_m (mM)	V_{max} ($\times 10^{-8}$ M·s^{-1})
$Pt_{50}Ag_{50}$	TMB	0.25	10.57
	H_2O_2	0.35	15.96
D-$Pt_{50}Ag_{50}$	TMB	0.38	33.04
	H_2O_2	0.86	34.75
HRP [36]	TMB	0.434	10
	H_2O_2	3.7	8.71

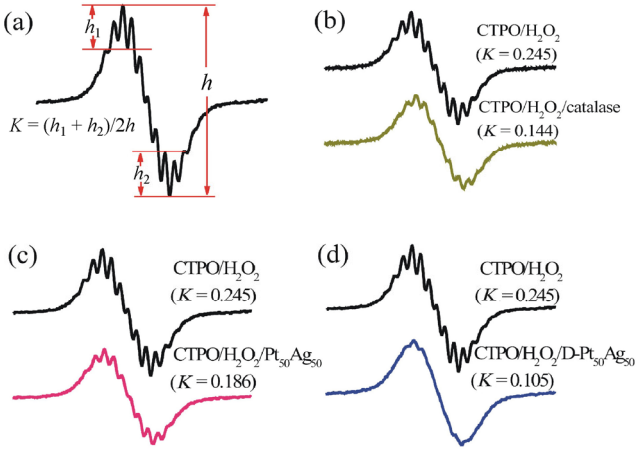

Figure 7 Enhanced catalase-like activity of the D-$Pt_{50}Ag_{50}$ NPs.

is the adsorption of molecular hydrogen, molecular oxygen, and hydroxyl ions on the surface of NPs (Scheme 1). Subsequently, hydrogen and oxygen are adsorbed through dissociative adsorption, i.e., hydrogen and oxygen atoms are directly bonded to the surface platinum atoms, while hydroxyl ions are involved in a simple charge transfer reaction. The surface-bound species further react with H_2O_2 in an Eley–Rideal mechanism [55, 56], releasing oxygen and water as products [57].

It is worth pointing out that numerous metal nanomaterials (e.g., Pt NPs) can catalyze H_2O_2 decomposition. As previously revealed [58, 59], the reactivity of surface metals greatly depends on their nature of d-bands, mainly the weighted center of the d-band (ε_d). For a higher lying d-band center, although the metals tend to bind adsorbates more strongly and make easy formation of M–OH bond, it is unfavorable for the breakage of M–OH bond and subsequent OH formation. However, the trend is just the opposite when the lying d-band center becomes lower [60].

$$H_2 + 2Pt \longrightarrow 2\ Pt\text{–}H \quad (1)$$

$$1/2O_2 + Pt \longrightarrow Pt\text{–}O \quad (2)$$

$$Pt + OH^- \longrightarrow Pt\text{–}(OH)_{ads} + e^- \quad (3)$$

$$Pt\text{–}(OH)_{ads} + H_2O_2 \longrightarrow Pt\text{–}(OOH)_{ads} + H_2O \quad (4)$$

$$Pt\text{–}H + H_2O_2 + e^- \longrightarrow Pt + H_2O + OH^- \quad (5)$$

$$Pt\text{–}(OOH)_{ads} + Pt\text{–}(H)_{ads} \longrightarrow 2Pt + O_2 + H_2 \quad (6)$$

$$Pt\text{–}O + 2\ Pt\text{–}H \longrightarrow Pt\text{–}H_2O + 2\ Pt \quad (7)$$

$$Pt\text{–}H_2O \longrightarrow Pt + H_2O \quad (8)$$

Scheme 1 The mechanism of H_2O_2 decomposition by D-$Pt_{50}Ag_{50}$.

Accordingly, the most active catalytic surface may be expected to possess a modest value of ε_d. For the pure Pt surface, the density functional theory (DFT) studies have shown that Pt–OH can be easily formed on the Pt surface because the value of ε_d of Pt is high. It means that a pure Pt surface is favorable for reaction (3) but unfavorable for reactions (4) and (5). Experimentally, these reactions should proceed efficiently to achieve an efficient decomposition of H_2O_2.

Similar to other Pt-based bimetallic NPs such as Pt/Pd and Pt/Cu NPs [54, 61], one of important factors for the high catalytic performance of D-$Pt_{50}Ag_{50}$ NPs in this study lies in the electronic effect, which derives from the d-band center shift of Pt. As evidenced by XPS in Fig. S5(c) (in the ESM), for the D-$Pt_{50}Ag_{50}$ NPs, there is a negative shift of the Pt $4f_{7/2}$ peak to lower BE (70.7 eV) compared to that of bulk Pt at BE of 71.0 eV. The decreased BE (0.3 eV) suggests that the electronic structure of Pt is modified, and the density of states at the Fermi level decreases upon filling Pt d-band. Thus, the changed density of states weakens the interaction of Pt and adsorbates, and this change facilitates reactions (3)–(5) and eventually increases the rate of decomposition of H_2O_2. It should be noted that the Ag $3d_{5/2}$ region also shifts to a lower BE (367.8 eV) with respect to that of metallic Ag (368 eV), which is shown in Fig. S5(d) in the ESM. A similar observation was reported for H_2O_2 decomposition with PVP-capped Rh/Au NPs [62], where the negative BE shifts for both Rh 3d and Au 4f regions were observed. The change in the BEs derived from the electron donation induced by carbonyl groups in PVP with the lone pair electrons. In our study, the change of BE in the Ag $3d_{5/2}$ can be ascribed to the existence of PAH because it was reported that PAH molecules can donate electrons from amino groups to noble metal NPs (e.g., Pt and Pd NPs), resulting in a negative shift of BE of metals compared to their standard values [63, 64]. With the interaction between the surfactant and metals, it is believed that the electrons from PAH molecules are transferred to Pt and Ag atoms within the present alloy-structured NPs. The result suggests that not only the element component but also the capping agent can change the electronic structure of the D- $Pt_{50}Ag_{50}$ NPs.

Additionally, in contrast to solid catalysts, the porous structure of D-$Pt_{50}Ag_{50}$ NPs not only endows a catalyst with the large surface area but also provides easy accessibility to active sites, thus accelerating the decomposition of H_2O_2. Notably, the Pt-enriched surface structure of the D-$Pt_{50}Ag_{50}$ NPs greatly increases atomic utilization efficiency of Pt.

3.4 Antibacterial effects of the dealloyed nanoparticles

Many biological reactions were completed with the enzymes. The catalytic capability of D-$Pt_{50}Ag_{50}$ NPs may result in new biological activities through effects on enzyme mimic activities or their catalytic activities in biological cells. Here, we studied the effects of D-$Pt_{50}Ag_{50}$ NPs on bacterial growth. The results (Fig. 8) revealed that when the concentration of D-$Pt_{50}Ag_{50}$ NPs was 20 $\mu g \cdot mL^{-1}$, about one half of the growth of two model bacteria (*E. coli* and *S. aureus*) was inhibited. After addition of H_2O_2, the growth of bacteria was nearly suppressed.

Further results on intracellular levels of lipid peroxidation and LDH release assays (see Fig. S9 in the ESM) indicate serious membrane oxidase damage and permeability of the bacterial membrane, resulting from synergistic effects of D-$Pt_{50}Ag_{50}$ NPs and H_2O_2.

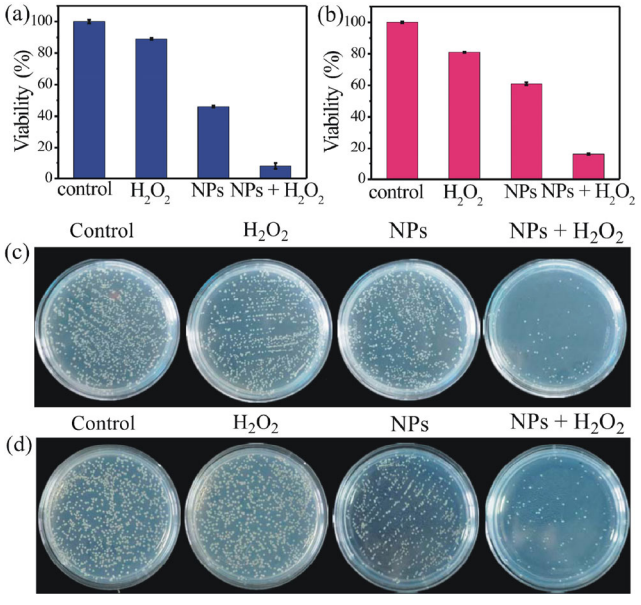

Figure 8 Cell viability of (a) *E. coli* and (b) *S. aureus*; the plate samples showing colonies of (c) *E. coli* and (d) *S. aureus*.

After that, we studied the relation between H_2O_2 concentration and antibacterial activity of D-$Pt_{50}Ag_{50}$ NPs. The results showed that survival rates decreased with an increase in the concentrations of H_2O_2 and NPs (see Fig. S10 in the ESM). The optimized H_2O_2 concentration for *E. coli* and *S. aureus* is 10 and 200 μM, respectively. Notably, some studies showed the graphene quantum dots [65] and mesoporous silica-supported Au NPs [66] with H_2O_2 possessed antibacterial capabilities. However, very high concentration of antibacterial agents (100 and 250 $\mu g \cdot mL^{-1}$) or H_2O_2 (1 and 10 mM) for *E. coli* and *S. aureus* were required in their experiments. Thus, the D-$Pt_{50}Ag_{50}$ NPs manifested excellent antibacterial activity in this work. To guide further design and development of this novel antibacterial agent, comprehensive research is needed to study the interaction between bacteria and NPs, which would be reported in due course.

4 Conclusions

In summary, porous Pt/Ag NPs with Pt-enriched structure were prepared by a chemical dealloying method and showed enhanced enzyme-mimic activities as well as excellent antibacterial effects. The results shown here provide an example of a highly active ORR catalyst as both a multifunctional enzyme mimic and a potential antibacterial agent. This work represents a significant step forward in the exploration of the relation between controlled synthesis of high-quality nanoalloys and their novel properties for multiple promising applications, including catalysts, biosensors, and biomedicine.

Acknowledgements

This work was supported by National Key Research and Development Program from the Ministry of Science and Technology of China (No. 2016YFC0207102) and National Natural Science Foundation of China (Nos. 21501034, 21573050 and 21503053). Financial support from Chinese Academy of Sciences (No. XDA09030303) and CAS Key Laboratory of Biological Effects of Nanomaterials and Nanosafety was also gratefully acknowledged. We thank associate Prof. Xun Hong from Center of Advanced Nanocatalysis in University of Science and Technology of China (USTC) for constructive discussion. We also thank Dr. Haijun Yang and Yayun Chen from Analysis Center of Department of Chemistry at Tsinghua University for help with ESR study. This work made use of the resources of the Beijing National Center for Electron Microscopy at Tsinghua University.

Electronic Supplementary Material: Supplementary material (additional characterization, catalytic results, antibacterial activity and related mechanism studies) is available in the online version of this article at http://dx.doi.org/10.1007/s12274-016-1395-0.

References

[1] Liang, Y. Y.; Li, Y. G.; Wang, H. L.; Zhou, J. G.; Wang, J.; Regier, T.; Dai, H. J. Co_3O_4 nanocrystals on graphene as a synergistic catalyst for oxygen reduction reaction. *Nat. Mater.* **2011**, *10*, 780–786.

[2] Cui, C.-H.; Li, H.-H.; Yu, J.-W.; Gao, M.-R.; Yu, S.-H. Ternary heterostructured nanoparticle tubes: A dual catalyst and its synergistic enhancement effects for O_2/H_2O_2 reduction. *Angew. Chem., Int. Ed.* **2010**, *49*, 9149–9152.

[3] Suntivich, J.; Gasteiger, H. A.; Yabuuchi, N.; Nakanishi, H.; Goodenough, J. B.; Shao-Horn, Y. Design principles for oxygen-reduction activity on perovskite oxide catalysts for fuel cells and metal-air batteries. *Nat. Chem.* **2011**, *3*, 546–550.

[4] Zhang, L.; Roling, L. T.; Wang, X.; Vara, M.; Chi, M. F.; Liu, J. Y.; Choi, S. I.; Park, J.; Herron, J. A.; Xie, Z. X. et al. Platinum-based nanocages with subnanometer-thick walls and well-defined, controllable facets. *Science* **2015**, *349*, 412–416.

[5] Wu, J. B.; Zhang, J. L.; Peng, Z. M.; Yang, S. C.; Wagner, F. T.; Yang, H. Truncated octahedral Pt_3Ni oxygen reduction reaction electrocatalysts. *J. Am. Chem. Soc.* **2010**, *132*, 4984–4985.

[6] Adzic, R. R.; Zhang, J.; Sasaki, K.; Vukmirovic, M. B.; Shao, M.; Wang, J. X.; Nilekar, A. U.; Mavrikakis, M.; Valerio, J. A.; Uribe, F. Platinum monolayer fuel cell electrocatalysts. *Top. Catal.* **2007**, *46*, 249–262.

[7] Sasaki, K.; Adzic, R. R. Monolayer-level Ru- and NbO_2-supported platinum electrocatalysts for methanol oxidation. *J. Electrochem. Soc.* **2008**, *155*, B180–B186.

[8] Sasaki, K.; Zhang, L.; Adzic, R. R. Niobium oxide-supported platinum ultra-low amount electrocatalysts for oxygen reduction. *Phys. Chem. Chem. Phys.* **2008**, *10*, 159–167.

[9] Stamenkovic, V.; Markovic, N. M.; Ross, P. N., Jr. Structure-relationships in electrocatalysis: Oxygen reduction and hydrogen oxidation reactions on Pt(111) and Pt(100) in solutions containing chloride ions. *J. Electroanal. Chem.* **2001**, *500*, 44–51.

[10] Stamenkovic, V. R.; Fowler, B.; Mun, B. S.; Wang, G. F.; Ross, P. N., Jr.; Lucas, C. A.; Marković, N. M. Improved oxygen reduction activity on $Pt_3Ni(111)$ via increased surface site availability. *Science* **2007**, *315*, 493–497.

[11] Yano, H.; Kataoka, M.; Yamashita, H.; Uchida, H.; Watanabe, M. Oxygen reduction activity of carbon-supported Pt-M (M = V, Ni, Cr, Co, and Fe) alloys prepared by nanocapsule method. *Langmuir* **2007**, *23*, 6438–6445.

[12] Marković, N. M.; Ross, P. N., Jr. Surface science studies of model fuel cell electrocatalysts. *Surf. Sci. Rep.* **2002**, *45*, 117–229.

[13] Gu, J.; Lan, G. X.; Jiang, Y. Y.; Xu, Y. S.; Zhu, W.; Jin, C. H.; Zhang, Y. W. Shaped Pt-Ni nanocrystals with an ultrathin Pt-enriched shell derived from one-pot hydrothermal synthesis as active electrocatalysts for oxygen reduction. *Nano Res.* **2015**, *8*, 1480–1496.

[14] Deogratias, N.; Ji, M. W.; Zhang, Y.; Liu, J. J.; Zhang, J. T.; Zhu, H. S. Core@shell sub-ten-nanometer noble metal nanoparticles with a controllable thin Pt shell and their catalytic activity towards oxygen reduction. *Nano Res*. **2015**, *8*, 271–280.

[15] Mani, P.; Srivastava, R.; Strasser, P. Dealloyed binary PtM_3 (M = Cu, Co, Ni) and ternary $PtNi_3M$ (M = Cu, Co, Fe, Cr) electrocatalysts for the oxygen reduction reaction: Performance in polymer electrolyte membrane fuel cells. *J. Power Sources* **2011**, *196*, 666–673.

[16] Oezaslan, M.; Strasser, P. Activity of dealloyed $PtCo_3$ and $PtCu_3$ nanoparticle electrocatalyst for oxygen reduction reaction in polymer electrolyte membrane fuel cell. *J. Power Sources* **2011**, *196*, 5240–5249.

[17] Strasser, P.; Koh, S.; Anniyev, T.; Greeley, J.; More, K.; Yu, C. F.; Liu, Z. C.; Kaya, S.; Nordlund, D.; Ogasawara, H. et al. Lattice-strain control of the activity in dealloyed core–shell fuel cell catalysts. *Nat. Chem.* **2010**, *2*, 454–460.

[18] Cui, C. H.; Li, H.-H.; Liu, X.-J.; Gao, M.-R.; Yu, S.-H. Surface composition and lattice ordering-controlled activity and durability of CuPt electrocatalysts for oxygen reduction reaction. *ACS Catal.* **2012**, *2*, 916–924.

[19] Liu, Z. Y.; Xin, H. L.; Yu, Z. Q.; Zhu, Y.; Zhang, J. L.; Mundy, J. A.; Muller, D. A.; Wagner, F. T. Atomic-scale compositional mapping and 3-dimensional electron microscopy of dealloyed $PtCo_3$ catalyst nanoparticles with spongy multi-core/shell structures. *J. Electrochem. Soc.* **2012**, *159*, F554–F559.

[20] He, D. S.; He, D. P.; Wang, J.; Lin, Y.; Yin, P. Q.; Hong, X.; Wu, Y.; Li, Y. D. Ultrathin icosahedral Pt-enriched nanocage with excellent oxygen reduction reaction activity. *J. Am. Chem. Soc.* **2016**, *138*, 1494–1497.

[21] Guo, S. J.; Li, D. G.; Zhu, H. Y.; Zhang, S.; Marković, N. M.; Stamenkovic, V. R.; Sun, S. H. FePt and CoPt nanowires as efficient catalysts for the oxygen reduction reaction. *Angew. Chem., Int. Ed.* **2013**, *52*, 3465–3468.

[22] Wang, D. L.; Yu, Y. C.; Xin, H. L.; Hovden, R.; Ercius, P.; Mundy, J. A.; Chen, H.; Richard, J. H.; Muller, D. A.; DiSalvo, F. J. et al. Tuning oxygen reduction reaction activity via controllable dealloying: A model study of ordered Cu_3Pt/C intermetallic nanocatalysts. *Nano Lett*. **2012**, *12*, 5230–5238.

[23] Wu, Y. E.; Cai, S. F.; Wang, D. S.; He, W.; Li, Y. D. Syntheses of water-soluble octahedral, truncated octahedral, and cubic Pt-Ni nanocrystals and their structure-activity study in model hydrogenation reactions. *J. Am. Chem. Soc.* **2012**, *134*, 8975–8981.

[24] Cui, C. H.; Gan, L.; Li, H. H.; Yu, S. H.; Heggen, M.; Strasser, P. Octahedral PtNi nanoparticle catalysts: Exceptional oxygen reduction activity by tuning the alloy particle surface composition. *Nano Lett.* **2012**, *12*, 5885–5889.

[25] Wang, Y.; Wan, D. H.; Xie, S. F.; Xia, X. H.; Huang, C. Z.; Xia, Y. N. Synthesis of silver octahedra with controlled sizes and optical properties via seed-mediated growth. *ACS Nano* **2013**, *7*, 4586–4594.

[26] Chang, C.-C.; Wu, H.-L.; Kuo, C.-H.; Huang, M. H. Hydrothermal synthesis of monodispersed octahedral gold nanocrystals with five different size ranges and their self-assembled structures. *Chem. Mater.* **2008**, *20*, 7570–7574.

[27] Zhu, E. B.; Li, Y. J.; Chiu, C.-Y.; Huang, X. Q.; Li, M. F.; Zhao, Z. P.; Liu, Y.; Duan, X. F.; Huang, Y. *In situ* development of highly concave and composition-confined PtNi octahedral with high oxygen reduction reaction activity and durability. *Nano Res*. **2016**, *9*, 149–157.

[28] Liu, X. W.; Wang, D. S.; Li, Y. D. Synthesis and catalytic properties of bimetallic nanomaterials with various architectures. *Nano Today* **2012**, *7*, 448–466.

[29] Polarz, S.; Smarsly, B. Nanoporous materials. *J. Nanosci. Nanotechnol.* **2002**, *2*, 581–612.

[30] Yang, H. C.; Hu, F.; Zhang, Y. J.; Shi, L. Y.; Wang, Q. B. Controlled synthesis of porous spinel cobalt manganese oxides as efficient oxygen reduction reaction electrocatalysts. *Nano Res*. **2016**, *9*, 207–213.

[31] Liu, Q. C.; Jiang, Y. S.; Xu, J. J.; Xu, D.; Chang, Z. W.; Yin, Y. B.; Liu, W. Q.; Zhang, X. B. Hierarchical Co_3O_4 porous nanowires as an efficient bifunctional cathode catalyst for long life Li-O_2 batteries. *Nano Res*. **2015**, *8*, 576–583.

[32] Huang, X. Q.; Zhu, E. B.; Chen, Y.; Li, Y. J.; Chiu, C.-Y.; Xu, Y. X.; Lin, Z. Y.; Duan, X. F.; Huang, Y. A facile strategy to Pt_3Ni nanocrystals with highly porous features as an enhanced oxygen reduction reaction catalyst. *Adv. Mater*. **2013**, *25*, 2974–2979.

[33] Zhou, B. B.; Sun, Z. F.; Li, D.; Zhang, T.; Deng, L.; Liu, Y.-N. Platinum nanostructures via self-assembly of an amyloid-like peptide: A novel electrocatalyst for the oxygen reduction. *Nanoscale* **2013**, *5*, 2669–2673.

[34] Yuwen, L.; Xu, F.; Xue, B.; Luo, Z. M.; Zhang, Q.; Bao, B. Q.; Su, S.; Weng, L. X.; Huang, W.; Wang, L. H. General synthesis of noble metal (Au, Ag, Pd, Pt) nanocrystal modified MoS_2 nanosheets and the enhanced catalytic activity of Pd-MoS_2 for methanol oxidation. *Nanoscale* **2014**, *6*, 5762–5769.

[35] El Mel, A.-A.; Boukli-Hacene, F.; Molina-Luna, L.; Bouts, N.; Chauvin, A.; Thiry, D.; Gautron, E.; Gautier, N.; Tessier, P.-Y. Unusual dealloying effect in gold/copper alloy thin films: The role of defects and column boundaries in the formation of nanoporous gold. *ACS Appl. Mater. Interfaces* **2015**, *7*, 2310–2321.

[36] Gao, L. Z.; Zhuang, J.; Nie, L.; Zhang, J. B.; Zhang, Y.; Gu, N.; Wang, T. H.; Feng, J.; Yang, D. L.; Perrett, S. et al. Intrinsic peroxidase-like activity of ferromagnetic nanoparticles. *Nat. Nanotechnol.* **2007**, *2*, 577–583.

[37] Tao, Y.; Lin, Y. H.; Huang, Z. Z.; Ren, J. S.; Qu, X. G. Incorporating graphene oxide and gold nanoclusters: A synergistic catalyst with surprisingly high peroxidase-like activity over a broad pH range and its application for cancer cell detection. *Adv. Mater.* **2013**, *25*, 2594–2599.

[38] Cai, S. F.; Qi, C.; Li, Y. D.; Han, Q. S.; Yang, R.; Wang, C. PtCo bimetallic nanoparticles with high oxidase-like catalytic activity and their applications for magnetic-enhanced colorimetric biosensing. *J. Mater. Chem. B* **2016**, *4*, 1869–1877.

[39] Marković, N. M.; Gasteiger, H. A.; Grgur, B. N.; Ross, P. N. Oxygen reduction reaction on Pt(111): Effects of bromide. *J. Electroanal. Chem.* **1999**, *467*, 157–163.

[40] Zhang, J.; Sasaki, K.; Sutter, E.; Adzic, R. R. Stabilization of platinum oxygen-reduction electrocatalysts using gold clusters. *Science* **2007**, *315*, 220–222.

[41] Cai, L.-T.; Chen, H.-Y. Electrocatalytic reduction of hydrogen peroxide at platinum microparticles dispersed in a poly(o-phenylenediamine) film. *Sens. Actuators B* 1**999**, *55*, 14–18.

[42] Wang, C.; Chi, M. F.; Wang, G. F.; van der Vliet, D.; Li, D. G.; More, K.; Wang, H.-H.; Schlueter, J. A.; Markovic, N. M.; Stamenkovic, V. R. Correlation between surface chemistry and electrocatalytic properties of monodisperse Pt_xNi_{1-x} nanoparticles. *Adv. Funct. Mater.* **2011**, *21*, 147–152.

[43] Zhang, L.-N.; Deng, H.-H.; Lin, F.-L.; Xu, X.-W.; Weng, S.-H.; Liu, A.-L.; Lin, X.-H.; Xia, X.-H.; Chen, W. *In situ* growth of porous platinum nanoparticles on graphene oxide for colorimetric detection of cancer cells. *Anal. Chem.* **2014**, *86*, 2711–2718.

[44] Su, L.; Feng, J.; Zhou, X. M.; Ren, C. L.; Li, H. H.; Chen, X. G. Colorimetric detection of urine glucose based $ZnFe_2O_4$ magnetic nanoparticles. *Anal. Chem.* **2012**, *84*, 5753–5758.

[45] Lin, T. R.; Zhong, L. S.; Guo, L. Q.; Fu, F. F.; Chen, G. N. Seeing diabetes: Visual detection of glucose based on the intrinsic peroxidase-like activity of MoS_2 nanosheets. *Nanoscale* **2014**, *6*, 11856–11862.

[46] Song, Y. J.; Qu, K. G.; Zhao, C.; Ren, J. S.; Qu, X. G. Graphene oxide: Intrinsic peroxidase catalytic activity and its application to glucose detection. *Adv. Mater.* **2010**, *22*, 2206–2210.

[47] Jiao, X.; Song, H. J.; Zhao, H. H.; Bai, W.; Zhang, L. C.; Lv, Y. Well-redispersed ceria nanoparticles: Promising peroxidase mimetics for H_2O_2 and glucose detection. *Anal. Methods* **2012**, *4*, 3261–3267.

[48] Dong, Y. L.; Zhang, H. G.; Rahman, Z. U.; Su, L.; Chen, X. J.; Hu, J.; Chen, X. G. Graphene oxide-Fe_3O_4 magnetic nanocomposites with peroxidase-like activity for colorimetric detection of glucose. *Nanoscale* **2012**, *4*, 3969–3976.

[49] Dong, Y. M.; Zhang, J. J.; Jiang, P. P.; Wang, G. L.; Wu, X. M.; Zhao, H.; Zhang, C. Superior peroxidase mimetic activity of carbon dots-Pt nanocomposites relies on synergistic effects. *New J. Chem.* **2015**, *39*, 4141–4146.

[50] Park, J.-N.; Shon, J. K.; Jin, M. S.; Hwang, S. H.; Park, G. O.; Boo, J.-H.; Han, T. H.; Kim, J. M. Highly ordered mesoporous α-Mn_2O_3 for catalytic decomposition of H_2O_2 at low temperatures. *Chem. Lett.* **2010**, *39*, 493–495.

[51] Lin, S.-S.; Gurol, M. D. Catalytic decomposition of hydrogen peroxide on iron oxide: Kinetics, mechanism, and implications. *Environ. Sci. Technol.* **1998**, *32*, 1417–1423.

[52] Kiyonaga, T.; Jin, Q. L.; Kobayashi, H.; Tada, H. Size-dependence of catalytic activity of gold nanoparticles loaded on titanium(IV) dioxide for hydrogen peroxide decomposition. *ChemPhysChem* **2009**, *10*, 2935–2938.

[53] Fan, J.; Yin, J.-J.; Ning, B.; Wu, X. C.; Hu, Y.; Ferrari, M.; Anderson, G. J.; Wei, J. Y.; Zhao, Y. L.; Nie, G. J. Direct evidence for catalase and peroxidase activities of ferritin-platinum nanoparticles. *Biomaterials* **2011**, *32*, 1611–1618.

[54] Hasnat, M. A.; Rahman, M. M.; Borhanuddin, S. M.; Siddiqua, A.; Bahadur, N. M.; Karim, M. R. Efficient hydrogen peroxide decomposition on bimetallic Pt-Pd surfaces. *Catal. Commun.* **2010**, *12*, 286–291.

[55] Prabhuram, J.; Manoharan, R. Investigation of methanol oxidation on unsupported platinum electrodes in strong alkali and strong acid. *J. Power Sources* **1998**, *74*, 54–61.

[56] Westbroek, P.; Temmerman, E. Mechanism of hydrogen peroxide oxidation reaction at a glassy carbon electrode in alkaline solution. *J. Electroanal. Chem.* **2000**, *482*, 40–47.

[57] Matsura, V. A.; Potekhin, V. V.; Platonov, V. V.; Tatsenko, O. M.; Ukraintsev, V. B.; Khokhryakov, K. A. Kinetics of reaction between oxygen and hydrogen in water in the presence of Pd(0)-containing compounds. *Russ. J. Gen. Chem.* **2003**, *73*, 1671–1675.

[58] Hammer, B.; Nørskov, J. K. Theoretical surface science and catalysis—Calculations and concepts. *Adv. Catal.* **2000**, *45*, 71–129.

[59] Greeley, J.; Nørskov, J. K.; Mavrikakis, M. Electronic structure and catalysis on metal surfaces. *Annu. Rev. Phys. Chem.* **2002**, *53*, 319–348.

[60] Zhang, J. L.; Vukmirovic, M. B.; Xu, Y.; Mavrikakis, M.; Adzic, R. R. Controlling the catalytic activity of Platinum-monolayer electrocatalysts for oxygen reduction with different substrates. *Angew. Chem., Int. Ed.* **2005**, *44*, 2132–2135.

[61] Lu, Y.; Ye, W. C.; Yang, Q.; Yu, J.; Wang, Q.; Zhou, P. P.; Wang, C. M.; Xue, D. S.; Zhao, S. Q. Three-dimensional hierarchical porous PtCu dendrites: A highly efficient peroxidase nanozyme for colorimetric detection of H_2O_2. *Sens. Actuators B* **2016**, *230*, 721–730.

[62] Zhang, H. J.; Deng, X. G.; Jiao, C. P.; Lu, L. L.; Zhang, S. W. Preparation and catalytic activities for H_2O_2 decomposition of Rh/Au bimetallic nanoparticles. *Mater. Res. Bull.* **2016**, *79*, 29–35.

[63] Xu, G.-R.; Han, S.-H.; Liu, Z.-H.; Chen, Y. The chemical functionalized platinum nanodendrites: The effect of chemical molecular weight on electrocatalytic property. *J. Power Sources* **2016**, *306*, 587–592.

[64] Fu, G. T.; Jiang, X.; Ding, L. F.; Tao, L.; Chen, Y.; Tang, Y. W.; Zhou, Y. M.; Wei, S. H.; Lin, J.; Lu, T. L. Green synthesis and catalytic properties of polyallylamine functionalized tetrahedral palladium nanocrystals. *Appl. Catal. B: Environ.* **2013**, *138–139*, 167–174.

[65] Sun, H. J.; Gao, N.; Dong, K.; Ren, J. S.; Qu, X. G. Graphene quantum dots-band-aids used for wound disinfection. *ACS Nano* **2014**, *8*, 6202–6210.

[66] Tao, Y.; Ju, E. G.; Ren, J. S.; Qu, X. G. Bifunctionalized mesoporous silica-supported gold nanoparticles: Intrinsic oxidase and peroxidase catalytic activities for antibacterial applications. *Adv. Mater.* **2015**, *27*, 1097–1104.